Modeling extended defect ({311} and dislocation) nucleation and evolution in silicon

Ibrahim Avci[a] and Mark E. Law
SWAMP Center, Department of Electrical Engineering, University of Florida, Gainesville, Florida, 32611

Erik Kuryliw, Antonio F. Saavedra, and Kevin S. Jones
SWAMP Center, Department of Materials Science, University of Florida, Gainesville, Florida, 32611

(Received 21 March 2003; accepted 12 December 2003)

End of range (EOR) defects are the most commonly observed defects in ultrashallow junction devices. They nucleate at the amorphous-crystalline interface upon annealing after amorphization due to ion implantation. EOR defects range from small interstitial clusters of a few atoms to {311} defects and dislocation loops. They are extrinsic defects and evolve during annealing. Li and Jones [Appl. Phys. Lett., **73**, 3748 (1998)] showed that {311} defects are the source of the projected range dislocation loops. In this article, the same theory is applied to EOR dislocation loops to model the nucleation and evolution of the loops. The model is verified with experimental data and accurately represents the nucleation, growth, and Ostwald ripening stages of dislocation loop evolution. The density and the number of interstitials trapped by dislocation loops are compared with the experimental results for several annealing times and temperatures. © *2004 American Institute of Physics.* [DOI: 10.1063/1.1645644]

I. INTRODUCTION

Ion implantation is the primary source of introducing impurity atoms into the silicon substrate due to the inherent controllability of the implant profile. However, crystal damage is unavoidable and consequently defects form for amorphizing implants. In order to repair the damage, postimplant anneals are required. During solid phase epitaxial regrowth of the amorphous layer, end of rage (EOR) defects form at the amorphous-crystalline interface.[1] These defects range from small interstitial clusters of a few atoms to {311} defects and dislocation loops.

Electrical characteristics of devices can be directly or indirectly affected by dislocation loops. Dislocation loops can increase the leakage current when they lie across the device junction.[2] They can also change the point defect concentration around the loop layer by emitting[3] and capturing[4] interstitials, thus causing enhanced/retarded dopant diffusion. In order to design better devices, it is necessary to perform predictive simulations of dopant diffusion after implantation and thermal annealing. This is only possible if the amplitude, depth, temperature, and time dependencies of the extended defects are modeled.

During the last few years, a great deal of work has been carried out in order to better describe the evolution of dislocation loops. The coarsening of EOR defects and the effects of the surface on EOR defects was investigated by Giles *et al.*[5] The growth and shrinkage of a single loop, or a periodic array of loops, due to the capture and emission of point defects was modeled by Borucki.[6] Analytic expressions were derived by Dunham[7] for the growth rate of the disk shaped extended defects. Lampin *et al.*[8] modeled the nucleation and the growth of the EOR dislocation loops. Their model was also used to study the anomalous diffusion of boron.[9,10] But, their model did not take into account interstitial cluster formations and the interaction between the {311} defects and dislocation loops.[11]

This article presents a model that covers the entire evolution of the point defect/implant damage to clusters, {311}s, and eventually, loops. Figure 1 schematically represents the model. The developed loop nucleation model assumes that excess interstitials are the source of the defects. Initially, UT-Marlowe[12] is used to calculate the excess interstitials and vacancies created in the silicon substrate due to ion implantation. Subsequently, interstitial and vacancy clusters such as di-interstitials (I_2), divacancies (V_2), and submicroscopic interstitial clusters (SMICs) are created upon annealing, and {311} defects are nucleated from SMICs. Some of these nucleated {311}s become thermally unstable and unfault to dislocation loops. {311}s become the source of dislocation loops.[1] Finally, while the remaining {311}s start dissolving, dislocation loops begin to evolve. The model describes the nucleation, growth, and Ostwald ripening stages of dislocation loop evolution with a single set of equations. Even though there are two types of dislocation loops, Frank loops with a Burgers vector of $a/3\langle 111\rangle$ and perfect loops with a Burgers vector of $a/2\langle 111\rangle$[13] for the chosen experimental conditions, Frank loops are the most numerous ones. In order to simplify the model, Frank loops are considered. Nevertheless, EOR defects are interstitial loops and the model is based on this fact.

II. MODEL

In order to model the evolution of dislocation loops accurately and efficiently, some assumptions need to be made. It is assumed that dislocation loop density and the average

[a]Present address: Integrated Systems Engineering, San Jose, California 95113; electronic mail: ibrahim.avci@ise.com

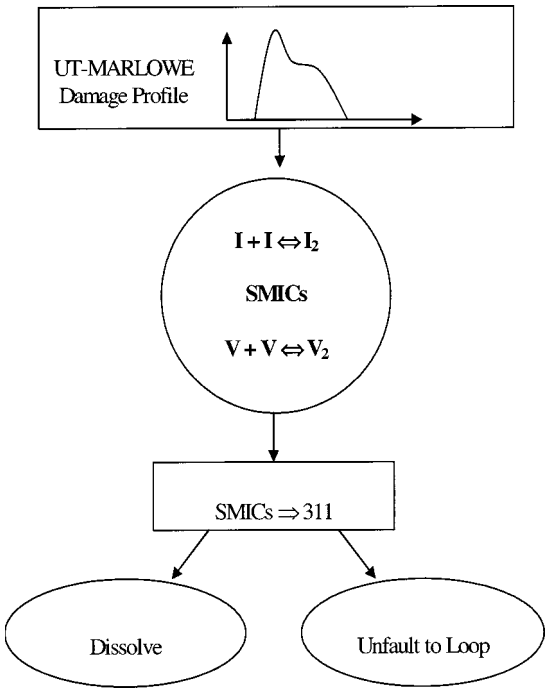

FIG. 1. Schematic representation of dislocation loop nucleation.

radius of loops follow a log normal distribution. It is also assumed that pressure from the dislocation loops can be calculated using lattice mismatch techniques.

A. Initial damage anneal

We use UT-Marlowe[12] to obtain the initial damage distribution for vacancies and interstitials. The profile is truncated at the damage threshold of $5.0\times10^{20}\,\mathrm{cm}^{-3}$. The amorphous layer is assumed to regrow instantaneously at the annealing temperature and is initialized to the thermal equilibrium concentration. We then apply a room temperature anneal to the damage beyond the amorphous-crystalline interface to simulate the cluster formation and recombination that occurs during the implant process itself. We allow formation of divacancies, di-interstitials, and recombination of vacancies and interstitials to occur. The few free interstitials that are left are assumed to be in small interstitial clusters based on insight from molecular dynamics simulations.[14] This results in a ''plus one'' like model[15]—most of the vacancies have recombined or clustered.

B. {311} formation and evolution

This initial damage distribution is then allowed to evolve. SMICs evolve into {311} defects when they capture either an interstitial or di-interstitial. In this initial interstitial rich region, the {311}s grow rapidly. The {311} model proposed by Law *et al.*[16] solves for the total number of interstitials in the defects (C_{311}) and the total number of defects (D_{311}).

The capture and release of intersititals on the {311} defects occur only at the end of the defects, and therefore are proportional to the number of defects, D_{311}. This provides two distinct results. First, individual defects dissolve at a nearly constant rate, since the dissolution is proportional only to the end size. The length of the defect does not determine the dissolution rate—there is no driving force for the Ostwald ripening of the {311} defects. This is supported by *in situ* annealing results reported in Ref. 16 and by the lack of change in size for implants below 80 keV reported in Saleh *et al.*[17] (Fig. 2).

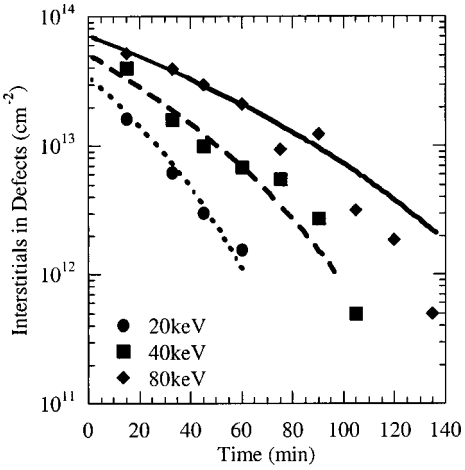

FIG. 2. Trapped interstitial concentration in {311} defects for different Si^+ implant energies with a $1\times10^{14}\,\mathrm{cm}^{-2}$ dose annealed at 750 °C. Data points are from Ref. 17 and fitted using the {311} model proposed by Law *et al.* (Ref. 16).

The second interesting result is that the defect ensemble decays at a rate that is dependent on size. The number of defects determines the decay rate. Consider two ensembles with the same number of interstitials, but with different sizes. The ensemble with the smaller size has more defects than the one with the larger size, and therefore will decay faster. The {311} defect population decays at a rate that is proportional to the interstitial loss rate and inversely proportional to the size of the defect. The size dependence accounts for ensembles of smaller defects dissolving faster than ensembles of larger defects and helps to get the correct implant energy dependence of dissolution rate.

C. Density of dislocation loops

It is known through the transmission electron microscopy (TEM) analysis that dislocation loops do not show a uniform radius and density distribution. Thus, a model that described the distribution of the loop sizes via a statistical function is needed. Through analysis of other researcher's work,[18,19] it is determined that log normal distribution function quantifies distribution of the loop size pretty well. The log normal probability function is given as

$$f_D(R)=\frac{D_{\mathrm{all}}}{SR\sqrt{2\pi}}e^{-(\ln R-M)^2/(2S^2)}, \tag{1}$$

where D_{all} is the total density of dislocation loops and R is the loop radius. S and M are the deviation and the mean of the log normal distribution.

TABLE I. Parameters used in the model.

Variable	Value
K_{VL} (loop-vacancy reaction rate)	0
K_{IL} (loop-interstitial reaction rate)	$K\times R_p\times 4\pi\times D_0\times a\times D_{\text{all}}$
K (fitting parameter)	$4.97\times 10^{14}\, e^{(-2.37/kT)}$ cm^2
D_{10} (diffusivity of interstitials)	$0.138\times e^{(-1.37/kT)}$ cm^2/s
a (Si lattice constant)	5.4×10^{-8} cm
K_R (coarsening rate)	$2.99\times 10^{-7}\, e^{(-1.93/kT)}$ cm^2/s
K_{311} ({311} unfaulting rate)	$360.59\, e^{(-1.2/kT)}$ s^{-1}

Since dislocation loops lie on the {111} plane and are circular with a radius of R, the number of interstitials bounded to these dislocation loops can be easily calculated as

$$N_{\text{all}}(R)=D_{\text{all}}(R)n_a\pi R^2, \tag{2}$$

where $D_{\text{all}}(R)$ is the density of dislocation loops with a radius of R and $n_a\,(1.5\times 10^{15}\,\text{cm}^{-2})$ is the atomic density of silicon atoms on the {111} plane. $N_{\text{all}}(R)$ represents the total number of interstitials bounded by these dislocation loops. The time derivative of Eq. (2) will give the change in the density of dislocation loops with time

$$\frac{dD_{\text{all}}(R)}{dt}=\frac{1}{\pi R_0^2 n_a}\frac{dN_{\text{all}}(R)}{dt}-\frac{2D_{\text{all}}(R)}{R}\frac{dR}{dt}. \tag{3}$$

The first term represents the nucleation rate of dislocation loops $N_{\text{rate}}^{D_{\text{all}}}$. R_0 is assumed to be the initial radius of the nucleated loop. The second term represents the Ostwald ripening process and can simply be written as[20]

$$\frac{dR}{dt}=\frac{K_R}{R}. \tag{4}$$

The constant, $K_R\,(\text{cm}^2/\text{s})$, is the coarsening rate of dislocation loops and is used as a fitting parameter in the simulations (Table I). If Eq. (4) is substituted into Eq. (3), the change in the density of dislocation loops with time becomes

$$\frac{dD_{\text{all}}(R)}{dt}=N_{\text{rate}}^{D_{\text{all}}}-\frac{2D_{\text{all}}(R)}{R^2}K_R. \tag{5}$$

The density of dislocation loops with smaller radii decreases faster than those with larger radii as seen in Eq. (5). Thus, smaller loops dissolve faster by emitting interstitials. These interstitials are absorbed by the bigger loops. Hence, bigger loops grow at the expense of smaller ones. Physically, this means that it is energetically more favorable for a large loop to increase in size and a small loop to dissolve, since it results in a reduction of the total interfacial and elastic energies.

D. Coarsening and dissolution of dislocation loops

Dislocation loops grow in size and reduce their density at annealing temperatures below 900 °C. Significant dissolution is not observed until 900. This regime is referred to as the ''coarsening'' regime. If the annealing temperature is over 900 °C, dislocation loops becomes thermally unstable and start dissolving by releasing interstitials.

The interaction between the loops and point defects is primarily reflected on the equilibrium concentration of point defects around the dislocation loop layer. The pressure dependent concentrations of interstitials and vacancies are calculated[7] as

$$C_I^*(P)=C_I^*(0)\exp\left(\frac{-P\Delta V_I}{kT}\right), \tag{6}$$

$$C_V^*(P)=C_V^*(0)\exp\left(\frac{P\Delta V_V}{kT}\right), \tag{7}$$

where P is the pressure, ΔV_I and ΔV_V are the elastic volume expansions susceptible to the external pressure effect on an interstitial and vacancy, k and T are the Boltzmann's constant and absolute temperature, respectively. ''0'' denotes the equilibrium concentration in the absence of external pressure. If the lattice is under compressive pressure, the equilibrium interstitial concentration will be less than its nominal value $C_I^*(0)$. If the lattice is under tensile pressure, then the equilibrium concentration of interstitials will be greater than its nominal value.

Growth and shrinkage of dislocation loops are determined by their interaction with point defects at the loop boundaries. The effective equilibrium concentration of interstitials (C_{Ib}) and vacancies (C_{Vb}) at the loop boundaries are given by Borucki[7] as

$$C_{Ib}=g_{\text{bc}}C_I^*(P)\exp\left(\frac{-\Delta E_f}{kT}\right), \tag{8}$$

$$C_{Vb}=g_{\text{bc}}^{-1}C_V^*(P)\exp\left(\frac{\Delta E_f}{kT}\right), \tag{9}$$

where g_{bc}[18] is a geometric factor which used to obtain the boundary conditions for this model from the formulation of the boundary condition for a single loops.[7] ΔE_f is the change in the defect formation energy due to the self-force of a dislocation loop during the emission and absorption process at its edge and is given by Gavazza *et al.*[21] as

$$\Delta E_f=-\frac{\mu b\Omega}{4\pi(1-\upsilon)R}\left[\ln\left(\frac{8R}{r_c}\right)-\frac{2\upsilon-1}{4\upsilon-4}\right], \tag{10}$$

where μ is the shear modulus, b is the magnitude of the Burgers vector of the loop, Ω is the atomic volume of silicon, r_c is the core radius of the loop, υ is the Poisson's ratio, and R is the radius of the dislocation loop.

The capture and emission rate of interstitials by the dislocation loops can be expressed in terms of the rates of emission and absorption of point defects at the loop layer boundaries modulated by a log normal distribution function. The rate also depends on the unfaulting rate of {311}s during the nucleation phase ($N_{\text{rate}}^{N_{\text{all}}}$) and can be expressed as

$$\frac{dN_{\text{all}}}{dt}=N_{\text{rate}}^{N_{\text{all}}}+K_{IL}\int_{0^+}^{\infty}(C_I-C_{Ib})f_D(R)dR - K_{VL}\int_{0^+}^{\infty}(C_V-C_{Vb})f_D(R)dR\Big|_{\substack{\text{at loop layer}\\ \text{boundaries}}}, \tag{11}$$

where K_{IL} is the constant of a reaction between the interstitials and the dislocation loop assemble, K_{VL} is a similar constant for vacancies. K_{IL} and K_{VL} are the function of the loop radius (R_p), loop density (D_{all}), and the diffusivity of interstitials (D_{I0}) and vacancies (D_{V0}), respectively (Table I). K_{IL} (cm^3/s) is one of the major fitting parameters used in the model. Physically, this determines the rate at which the interstitials react with the dislocation loop ensemble. C_I and C_V are the concentration of interstitials and vacancies. It is apparent that if the concentration of interstitials at the loop boundaries is greater than the effective equilibrium concentration of interstitials at the loop boundaries, loops will absorb interstitials. If the reverse is true, then the loops will emit interstitials. Modulating the emission and absorption rate by a log normal distribution function allows us to include the effects of all dislocation loops in the loop layer.

Since the Si surface can also affect the evolution of EOR defects by trapping interstitials, a simple interstitial flux to the surface with a high surface recombination rate is used to model the surface as a sink for interstitials.

When a {311} defect unfaults to form a dislocation loop, the number of interstitials bounded by that {311} is transferred to the unfaulted loop. This can be shown as

$$N_{\text{rate}}^{N_{\text{all}}} = K_{311} C_{311}, \tag{12}$$

where K_{311} (in units of s^{-1}, Table I) is the rate at which {311}s unfault to dislocation loops and C_{311} is the concentration of interstitials trapped by {311}s. A similar expression can be derived for $N_{\text{rate}}^{D_{\text{all}}}$ as well. Since, only the first term of Eq. (11) is related to the loop nucleation, $N_{\text{rate}}^{D_{\text{all}}}$ becomes

$$N_{\text{rate}}^{D_{\text{all}}} = \frac{K_{311} C_{311}}{\pi R_0^2 n_a}, \tag{13}$$

where

$$\pi R_0^2 n_a = \frac{C_{311}}{D_{311}}. \tag{14}$$

D_{311} is the density of {311} defects. If Eq. (14) is substituted in Eq. (13), the nucleation rate of dislocation loops can simply be written as

$$N_{\text{rate}}^{D_{\text{all}}} = K_{311} D_{311}. \tag{15}$$

In the simulations, K_{311} parameter is used as a fitting parameter to calibrate the simulations. Figure 3 shows the change in the nucleation rate ($N_{\text{rate}}^{D_{\text{all}}}$) with time. The rate is very high at short times when the excess interstitial concentration is high and {311}s are still nucleating. The nucleation rate diminishes as time progresses.

The total number of interstitials bound by all loops in the loop layer is given as

$$N_{\text{all}} = \int_{0^+}^{\infty} n_a \pi R^2 D_{\text{all}} f_D(R)\, dR, \tag{16}$$

$$N_{\text{all}} = D_{\text{all}} \pi n_a e^{2S^2 + 2M}. \tag{17}$$

Since experiments for the evolution of loops usually focus on the average radius of the loop distribution, the loop radius R in Eqs. (5) and (11) can be substituted with an average loop radius R_p. If the normal distribution mean (μ) is assumed to be the average radius (R_p) of the loop distribution, log-normal-deviation (S) and log-normal-mean (M) can be written as

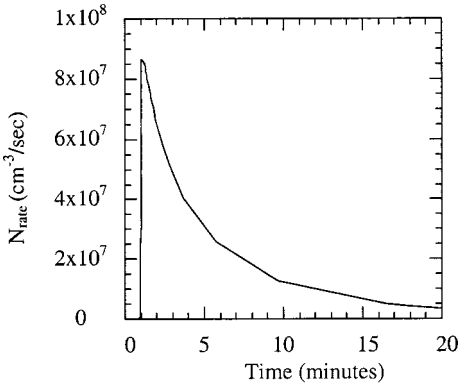

FIG. 3. Dislocation nucleation rate $N_{\text{rate}}^{D_{\text{all}}}$ change with time.

$$S = \ln\left[1 + \left(\frac{\sigma}{R_p}\right)^2\right]^{1/2}, \tag{18}$$

$$M = \ln\left(\frac{N_{\text{all}}}{D_{\text{all}} \pi n_a}\right)^{1/2} - S^2. \tag{19}$$

The relation between σ and R_p can be extracted statistically from various TEM data[18,19,22] as an analytic function of R_p (cm) as follows:

$$\frac{\sigma}{R_p} = 0.33 + 5 \times 10^4 R_p. \tag{20}$$

III. EXPERIMENTAL AND SIMULATION RESULTS

A. Experimental details

Single crystal Czochralski silicon wafers (⟨100⟩ orientation) were used as the starting material. Si^+ ions were implanted at either 80 or 40 keV at a dose of $2 \times 10^{15}\,\text{cm}^{-2}$. Under these implant conditions, a continuous amorphous layer forms. After the implant, the entire wafer was capped with thick SiO_2 before the anneal process to limit any oxidation in the inert ambient. Prior to annealing, cross-sectional TEM (XTEM) measurements were performed to determine the location of the amorphous-crystalline interface. The wafers were cut into smaller pieces and annealed in a nitrogen ambient at 700 and 750 °C. Annealing times were chosen to be 30, 60, 90, 120, and 240 min for 700 °C anneals and 15, 30, 60, 90, and 120 min for 750 °C anneals. The annealing times and temperatures were chosen so that the nucleation and evolution of {311}s and dislocation loops would be slow. This allowed the simultaneous observation of the changes in {311} and EOR dislocation densities for longer annealing times at these temperatures. After annealing, the cap oxide for all the samples were removed by HF dip before mechanical and jet etching. The total loop density is obtained from the plan view TEM (PTEM) studies by considering both Frank loops and perfect loops. By assuming a circular loop, the radius of each loop or partial loop was measured along its longest axis and the corresponding loop

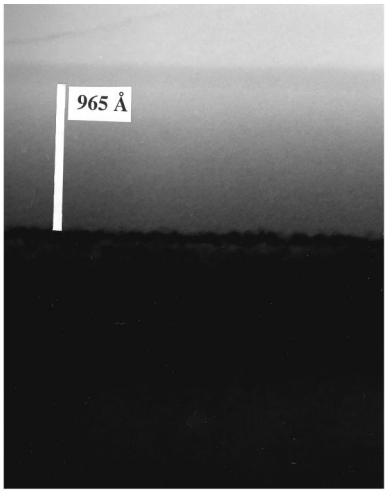

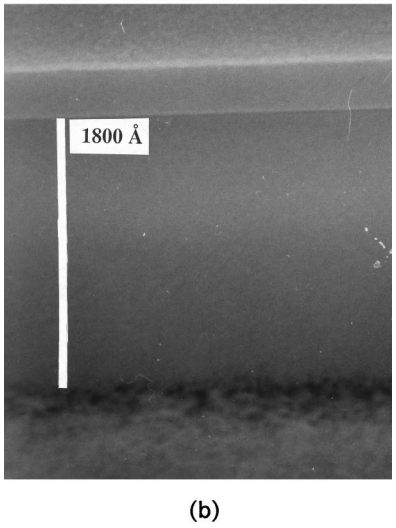

FIG. 4. Weak beam dark-field XTEM images of (a) 40 and (b) 80 keV Si^+ implanted Si to a dose of $2\times10^{15}\,cm^{-2}$ before furnace anneals.

area was calculated. The total number of interstitials bound by the loops are estimated by multiplying the fraction of loop area by the atomic density of atoms on the {111} plane.

The total {311} density and total number of interstitials bound by the {311}s were also measured from the plan view TEM studies.

B. Experimental results

The XTEM micrographs of 40 and 80 keV Si^+ implants at a dose of $2\times10^{15}\,cm^{-2}$ before furnace anneals are shown in Fig. 4. The amorphous-crystalline $(a-c)$ interface is located around 965 and 1800 Å for 40 and 80 keV samples, respectively. The XTEM pictures show that a continuous amorphous silicon region extends to the surface. End of range defects form at around the depth of the original amorphous-crystalline interface upon subsequent furnace annealing.

Figures 5 and 6 represent the PTEM pictures of the 40 keV samples after furnace anneals at 700 and 750 °C for various annealing times. The g_{220} reflection was used to acquire all the PTEMs under weak beam dark-field imaging conditions. It is observed that when dislocation loops and {311} defects are present at the same time, it is difficult to distinguish an elongated loop from a {311} defect. In order to obtain an accurate count of defects, PTEM pictures were taken with plus $(+)$ and minus $(-)$ g reflections. Since the small burgers vector associated with the {311} defect coupled with its narrow with means that the defects in weak beam appear as a single line whether they are in or outside contrast. Only when they unfault to loops and the burgers vector increase significantly is it possible for the outside contrast to show split pairs of lines, and identify them as extrinsic loops. Those studies showed that the elongated defects at longer annealing times in all samples were dislocation loops. It is observed from Figs. 5 and 6 that {311} defects nucleate and

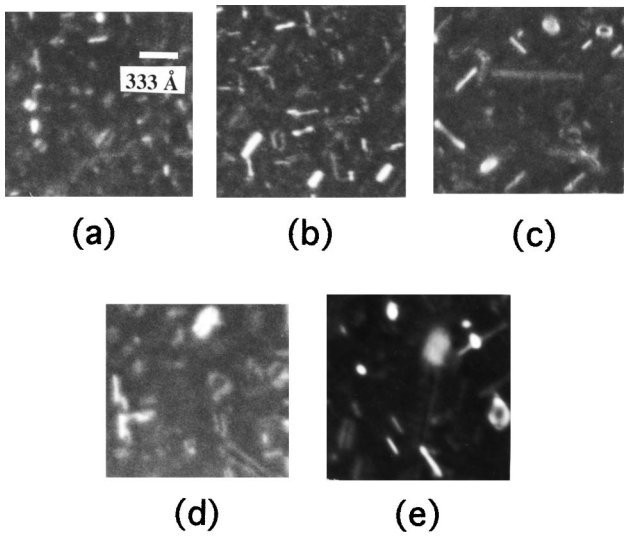

FIG. 5. Weak beam dark-field plan view TEM images of 40 keV Si^+ implanted Si to a dose of $2\times10^{15}\,cm^{-2}$, after an anneal at 700 °C for (a) 30, (b) 60, (c) 90, (d) 120, and (e) 240 min in N_2.

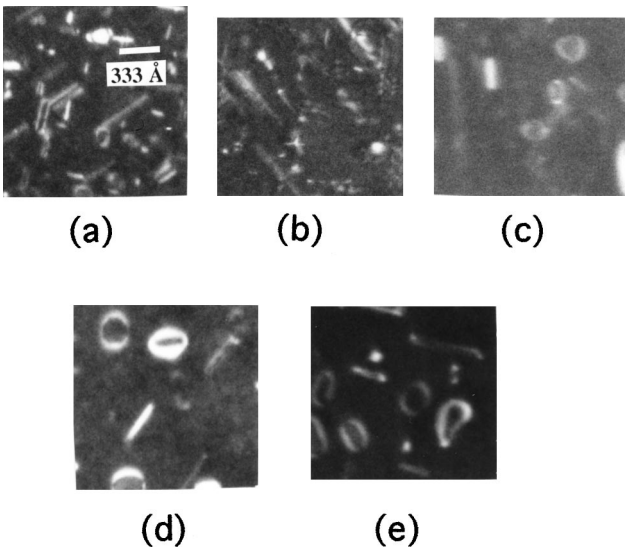

FIG. 6. Weak beam dark-field plan view TEM images of 40 keV Si^+ implanted Si to a dose of $2\times10^{15}\,cm^{-2}$, after an anneal at 750 °C for (a) 15, (b) 30, (c) 60, (d) 90, and (e) 120 min in N_2.

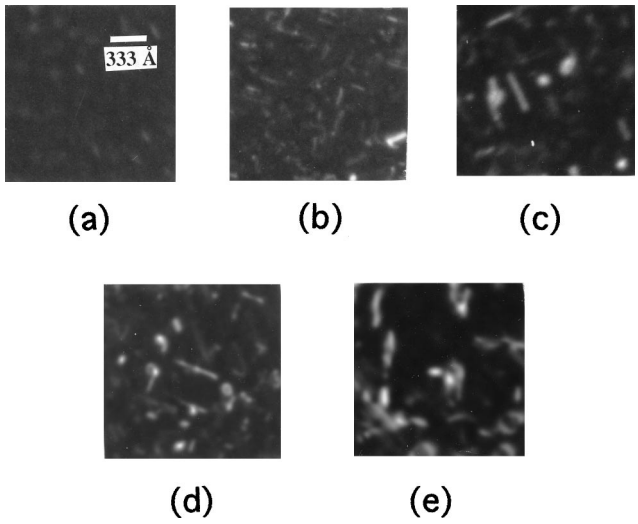

FIG. 7. Weak beam dark-field plan view TEM images of 80 keV Si^+ implanted Si to a dose of $2\times10^{15}\,cm^{-2}$, after an anneal at 700 °C for (a) 30, (b) 60, (c) 90, (d) 120, and (e) 240 min in N_2.

dissolve very fast at all anneal temperatures and times. The dissolution rate of {311} defects is slower at 700 °C than at 750 °C. No {311} defects are observed after annealing for 120 and 90 min at 700 and 750 °C, respectively. It is also observed that dislocation loops nucleate at a slower rate than {311} defects. The density of dislocation loops increases at short times at 700 °C. Then, it starts decreasing. The density of dislocation loops decreases at a faster rate at 750 °C than it does at 700 °C. While smaller loops dissolve, bigger loops grow (Ostwald ripening). The loops are smaller in size at the low annealing temperature. The same trends can be observed in the density of {311}s and dislocation loops for the samples implanted with 80 keV Si^+ to a dose of $2\times10^{15}\,cm^{-2}$ in Figs. 7 and 8. Although Fig. 7 shows the 80 keV sample annealed for 30 min at 700 °C, the defects observed in the TEM are too small to count with any reasonable accuracy.

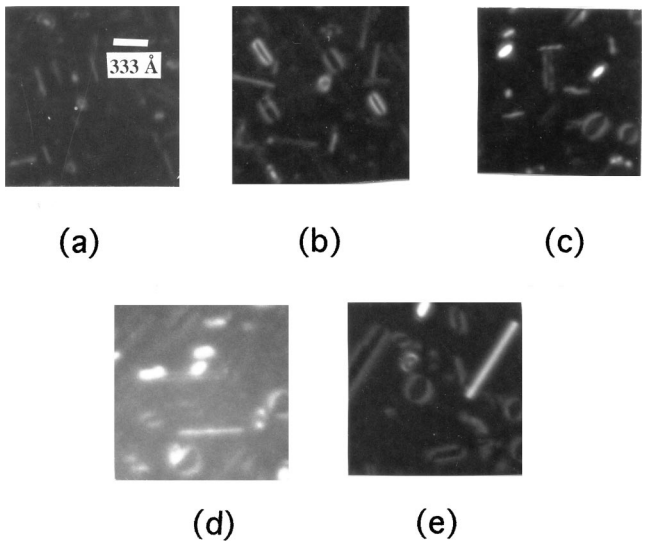

FIG. 8. Weak beam dark-field plan view TEM images of 80 keV Si^+ implanted Si to a dose of $2\times10^{15}\,cm^{-2}$, after an anneal at 750 °C for (a) 15, (b) 30, (c) 60, (d) 90, and (e) 120 min in N_2.

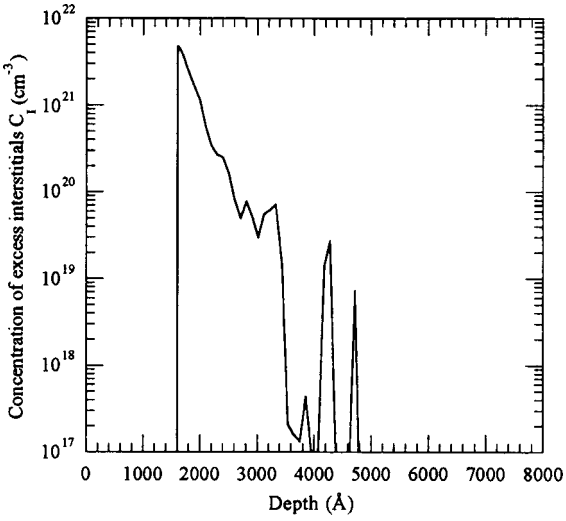

FIG. 9. Initial truncated excess interstitial concentration after an implantation of Si^+ with a dose of $2\times10^{15}\,cm^{-2}$ and energy of 80 keV.

C. Simulation results

Excess interstitial and vacancy profiles are generated for each implant dose and energy using UT-Marlowe with a kinetic accumulative damage model. UT-Marlowe output files estimate the amorphous depths to be around 1600 and 950 Å for 80 and 40 keV implants, respectively. The excess interstitial concentration is truncated at the $a-c$ interface and set to the equilibrium interstitial concentration in the amorphous region, Fig. 9. Excess vacancy profiles are obtained in a similar way for all simulations. These excess interstitials and vacancies provide the basis for the nucleation of I_2s, V_2s, and SMICs, eventually leading to the nucleation of {311}s and dislocation loops.

Figure 10 represents the changes in defect densities with time at an anneal temperature of 700 °C after implantation of

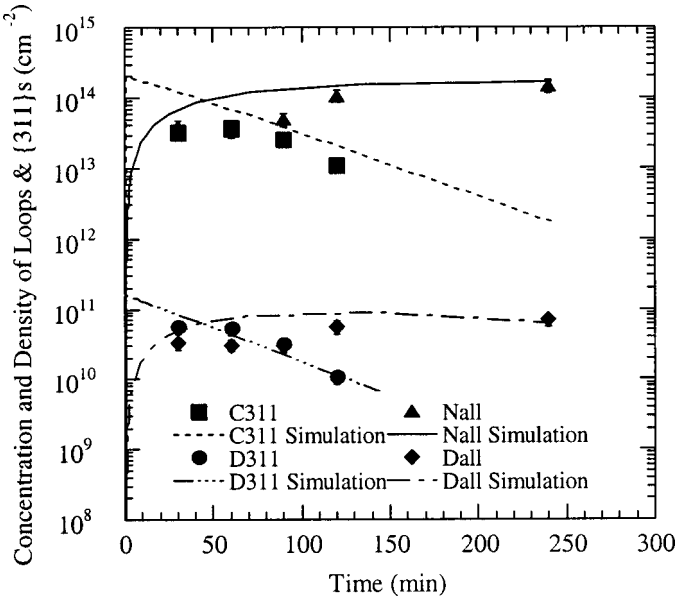

FIG. 10. Changes in defect densities with time at 700 °C after implantation of Si^+ with a dose of $2\times10^{15}\,cm^{-2}$ and energy of 40 keV. The symbols are experimental results and the lines are simulation results.

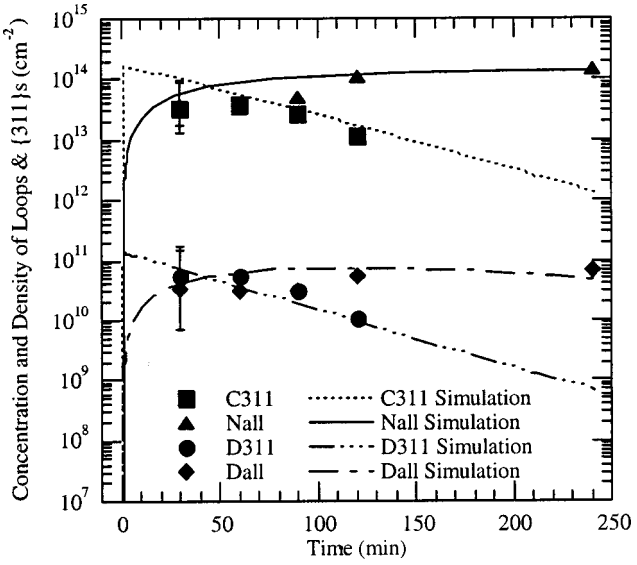

FIG. 11. Changes in defect densities with time at 700 °C after implantation of Si^+ with a dose of $2\times10^{15}\,cm^{-2}$ and energy of 40 keV. The symbols are experimental results and the lines are simulation results. Error bars are included to indicate simulation results are within experimental error.

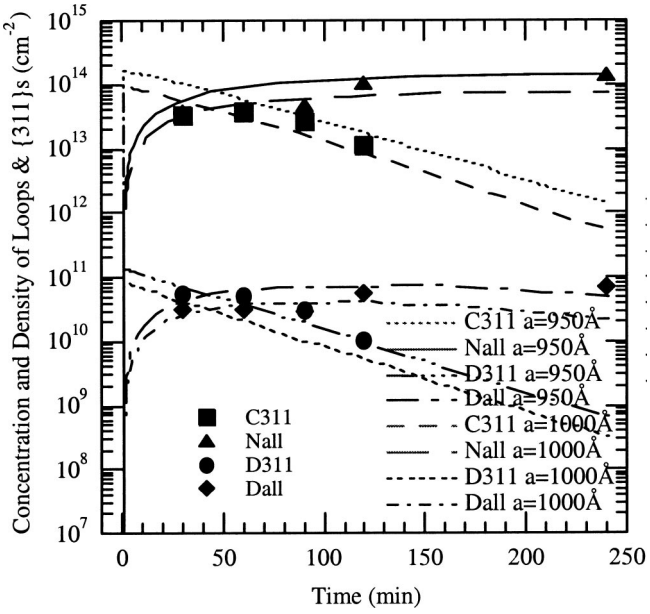

FIG. 12. Changes in defect densities with time at 700 °C after implantation of Si^+ with a dose of $2\times10^{15}\,cm^{-2}$ and energy of 40 keV. The symbols are experimental results and the lines are simulation results. Amorphous depth is set to 950 and 1000 Å as initial condition for two different simulations.

Si^+ with a dose of $2\times10^{15}\,cm^{-2}$ and energy of 40 keV. The symbols represent the experimental data and the lines represent the simulation results. As seen from the data, density of {311}s, D_{311}, and the number of interstitials bounded by {311}s, C_{311}, decrease with increasing anneal time. C_{311} and D_{311} show an exponential decay. Meanwhile, the density of dislocation loops, D_{all}, and the number of interstitials bound by loops, N_{all}, increase with increasing time. There is no significant change in the loop density after an initial 60 min anneal, while N_{all} continues to increase. If the simulation results are considered, it is easy to see that D_{311} and C_{311} increase very rapidly in short times and then begin decreasing. It is also obvious that the nucleation of dislocation loops is slower than the nucleation of {311}s since the loops nucleate from unfaulted {311}s. In Fig. 10, it is possible to observe two of the three distinct stages of loop nucleation and evolution. At short anneal times, both N_{all} and D_{all} increase rapidly when the nucleation rate is high. This is usually referred to as the nucleation stage. The nucleation stage is followed by the pure growth stage. During this stage, D_{all} stays almost constant while N_{all} keep increasing since the excess interstitial concentration is still high. In the third stage, Ostwald ripening occurs and the loops go into this stage when the excess interstitial concentration drops. D_{all} starts decreasing and N_{all} stays constant during this stage. The bigger loops grow at the expense of smaller ones.

Simulation results are mostly in good agreement with the experimental data. The biggest discrepancy between the data and simulation is seen at the shortest anneal time due to the smaller defect sizes seen in TEM pictures. If the defect size is too small, it becomes harder to distinguish {311} defects from dislocation loops and the error increases. Therefore, the defects for the shortest anneal time are recounted to obtain the error bars shown in Fig. 11. The upper bound on the error is obtained by assuming that all defects are either dislocation loops or {311}s. The recount was done aggressively to include every small defect. The lower bound on the error bar is obtained by pursuing a nonaggressive approach where only the defects that are clearly {311}s or loops are recounted. The results are shown in Fig. 11. Error bars show that simulation results lie within range of experimental error.

Initial conditions used in the simulations also play an important role. Figure 12 shows the changes in defect density with time for the case of 700 °C, 40 keV. It also shows two different simulation results with two different initial conditions. The excess interstitial and vacancy profiles are obtained by assuming two different amorphization depths. In the first case, the amorphous depth is set to 950 Å and the excess interstitial and vacancy profiles are truncated using this amorphous depth. Then the simulation is carried out. In the second case, amorphous depth is set to 1000 Å and the same procedure is repeated. As seen in Fig. 12, the difference between the two simulations could be quite significant. Increasing the amorphous depth by 50 Å shifts all the profiles in negative *y* directions. This is due to the fact that increasing the amorphous depth reduces the number of excess interstitials available for the nucleation of {311}s and dislocation loops. If Fig. 9 is closely examined, it can be seen that the slope of the excess interstitial profile is quite steep around the amorphous depth. Even if the amorphous depth is changed by 50 Å, the change in the number of excess interstitials will be very significant.

Figure 13 shows the change in defect density with time for the 750 °C, 40 keV sample. Experimental and simulation results have all the characteristics explained earlier. The nucleation rate of dislocation loops and dissolution rates of {311}s at 750 °C are faster than that at 700 °C.

The changes in defect densities with time at 700 and 750 °C for 80 keV samples are shown in Figs. 14, 15, and 16.

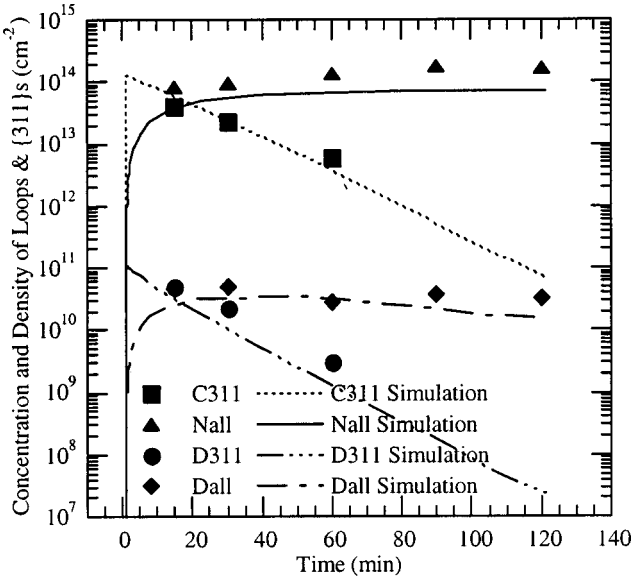

FIG. 13. Changes in defect densities with time at 750 °C after implantation of Si^+ with a dose of $2\times10^{15}\,cm^{-2}$ and energy of 40 keV. The symbols are experimental results and the lines are simulation results.

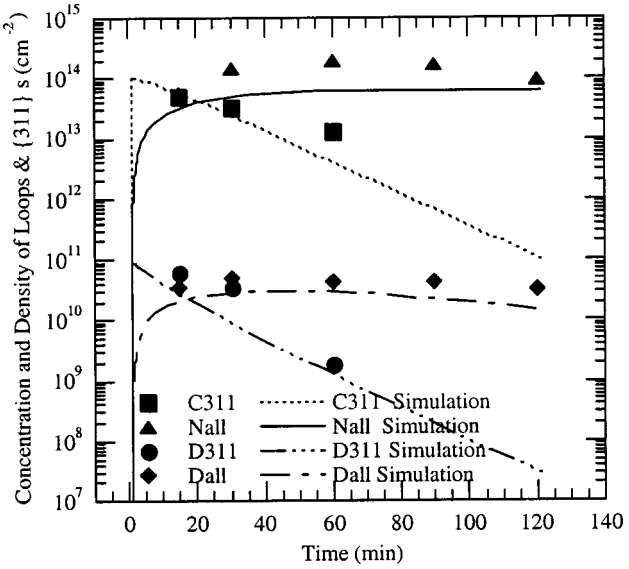

FIG. 15. Changes in defect densities with time at 750 °C after implantation of Si^+ with a dose of $2\times10^{15}\,cm^{-2}$ and energy of 80 keV. The symbols are experimental results and the lines are simulation results.

The same trends observed in defect densities in 40 keV samples are observed for these samples as well. 80 keV samples generate deeper loop layers than the 40 keV samples. The surface effects on defects for two cases (700 and 750 °C) would be different. Simulation results are in good agreement with the experimental data in both sample sets. This shows that surface effects are also modeled correctly in the loop model.

The variations in defect densities with time at 750 °C for 80 keV, samples with two different simulation results are represented in Fig. 16. The amorphous depths are set to 1600 and 1650 Å to generate excess interstitial and vacancy profiles as two different initial conditions for simulations as explained earlier. The importance of initial conditions used for the simulations is emphasized in this figure one more time since the shift in the profiles can be significant.

IV. SUMMARY

Since amorphization commonly occurs during ion implantation, EOR defects are hard to avoid upon annealing. Therefore, EOR defects are very common in today's technologies. It is very important to be able to predict their size and density using physical models in order to design better devices. This model assumes that all the loops come from

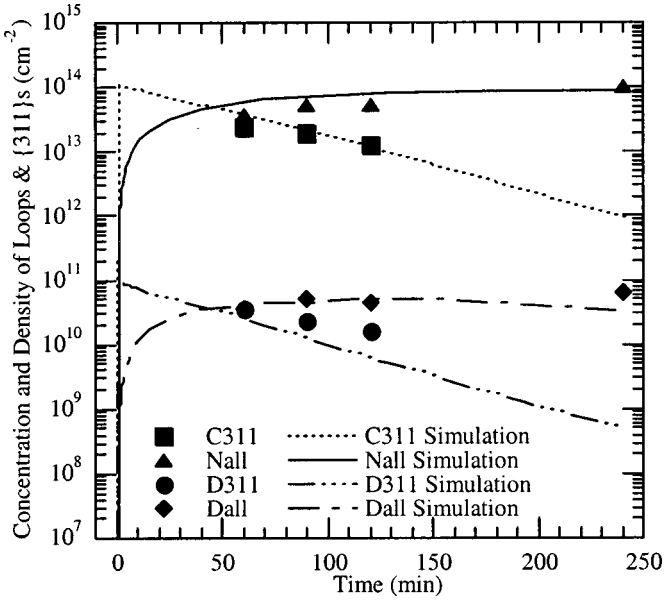

FIG. 14. Changes in defect densities with time at 700 °C after implantation of Si^+ with a dose of $2\times10^{15}\,cm^{-2}$ and energy of 80 keV. The symbols are experimental results and the lines are simulation results.

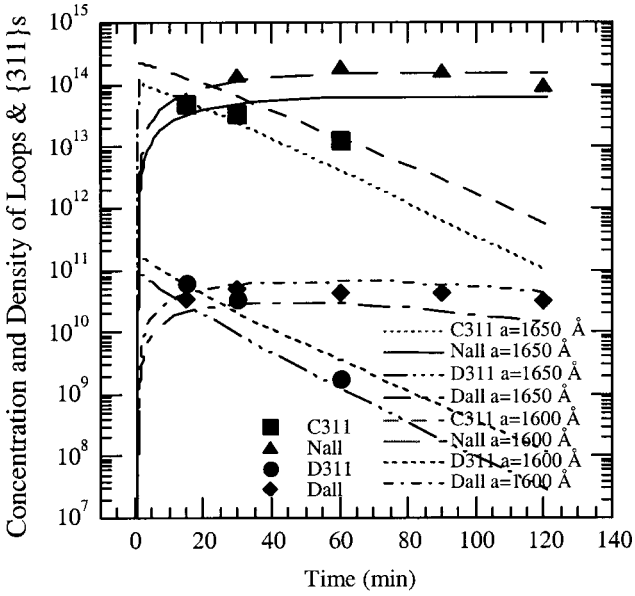

FIG. 16. Changes in defect densities with time at 750 °C after implantation of Si^+ with a dose of $2\times10^{15}\,cm^{-2}$ and energy of 80 keV. The symbols are experimental results and the lines are simulation results. Amorphous depth is set to 1650 and 1600 Å as initial condition for two different simulations.

unfaulting of {311} defects. The excess interstitial and vacancy populations due to ion implantation are obtained from UT-Marlowe. They are utilized to generate interstitial and vacancy clusters, eventually leading to the nucleation of {311}s and dislocation loops. The model is verified by two sets of experiments that are designed to investigate the nucleation and evolution of EOR defects.

Simulations are carried out using UT-MARLOWE damage profiles. It is observed that the experiments and simulations are in good agreement. Performing the experiment at two different temperatures helped to calibrate the model and determine the temperature dependence of the fitting parameters used in the model. Results support the idea that {311}s are the source of the dislocation loops. The importance of the initial conditions on the simulations is also emphasized. A summary of the fitting parameters used in the model is given in Table I.

ACKNOWLEDGMENTS

The authors would like to thank Intel and SRC for providing the funding and material for this research.

[1] K. S. Jones, S. Prussin, and E. R. Weber, Appl. Phys. A: Solids Surf. **45**, 1 (1988).
[2] M. Miyake and M. Takahashi, J. Electrochem. Soc. **144**, 1020 (1997).
[3] R. Y. S. Huang and R. W. Dutton, J. Appl. Phys. **74**, 5821 (1993).
[4] J. Liu, M. E. Law, and K. S. Jones, Solid-State Electron. **38**, 1305 (1995).
[5] L. F. Giles, M. Omri, B. de Mauduit, A. Claverie, D. Skarlatos, D. Tsoukalas, and A. Nejim, Nucl. Instrum. Methods Phys. Res. B **148**, 273 (1999).
[6] L. Borucki, IEEE NUPAD IV, 27 (1992).
[7] S. T. Dunham, Appl. Phys. Lett. **63**, 464 (1993).
[8] E. Lampin and V. Senez, Nucl. Instrum. Methods Phys. Res. B **147**, 13 (1999).
[9] E. Lampin, V. Senez, and A. Claverie, J. Appl. Phys. **85**, 8137 (1999).
[10] E. Lampin, V. Senez, and A. Claverie, Mater. Sci. Eng., B **71**, 155 (2000).
[11] J. Li and K. S. Jones, Appl. Phys. Lett. **73**, 3748 (1998).
[12] B. Obradovic, G. Wang, Y. Chen, D. Li, C. Snell, and A. F. Tasch, UT-MARLOWE 5.0 with Tomcat user manual, 1999.
[13] B. de Mauduit, L. Laanab, C. Bergaud, M. M. Faye, A. Martinez, and A. Claverie, Nucl. Instrum. Methods Phys. Res. B **84**, 190 (1994).
[14] M. J. Cuturla, T. D. delaRubia, L. A. Marques, and G. H. Gilmer, Phys. Rev. B **54**, 16683 (1996).
[15] M. D. Giles, J. Electrochem. Soc. **138**, 1160 (1991).
[16] M. E. Law and K. S. Jones, Tech. Dig.-Int. Electron Devices Meet., **2000**, 511.
[17] H. Saleh, M. E. Law, S. Bharatan, K. S. Jones, W. Krishnamoorthy, and T. Buyuklimanli, Appl. Phys. Lett. **77**, 112 (2000).
[18] H. Park, K. S. Jones, and M. E. Law, J. Electrochem. Soc. **141**, 759 (1994).
[19] S. Chaudhry, J. Liu, K. S. Jones, and M. E. Law, Solid-State Electron. **38**, 1313 (1995).
[20] C. Bonofas, D. Mathiot, and A. Claverie, J. Appl. Phys. **83**, 3008 (1998).
[21] S. D. Gavazza and D. M. Barnett, J. Mech. Phys. Solids **24**, 171 (1976).
[22] R. Raman, M. E. Law, V. Krishnamoorthy, K. S. Jones, and S. B. Herner, Appl. Phys. Lett. **74**, 1591 (1999).